

# APPLICATION OF PANSHARPENING ALGORITHMS FOR THE FUSION OF RAMAN AND CONVENTIONAL BRIGHTFIELD MICROSCOPY IMAGES

Ch. Pomrehn<sup>1</sup>, D. Klein<sup>2</sup>, A. Kolb<sup>3</sup>, P. Kaul<sup>2</sup>, R. Herpers<sup>1,4,5</sup>

<sup>1</sup>Institute of Visual Computing, Bonn-Rhein-Sieg University of Applied Sciences, Germany

<sup>2</sup>Institute of Safety and Security Research, Bonn-Rhein-Sieg University of Applied Sciences, Germany

<sup>3</sup>Institute for Vision and Graphics, University of Siegen, Germany

<sup>4</sup>Faculty of Computer Science, University of New Brunswick, Canada

<sup>5</sup>Lassonde School of Engineering, York University, Canada

## ABSTRACT

This contribution investigates the application of established pansharpening algorithms for the fusion of hyperspectral images from Raman microspectroscopy and panchromatic images from conventional brightfield microscopy. Seven different methods based on multiresolution analysis and component substitution were applied and evaluated through visual assessment and quantitative quality measures at full and reduced resolution. The results indicate that, among the considered concepts, multiresolution methods are the more promising approaches for a physically and chemically meaningful fusion of the considered modalities. Here, pansharpening based on high-pass filtering led to the best results.

**Index Terms**— Hyperspectral image, pansharpening, image fusion, Raman microscopy, brightfield microscopy,

## 1. INTRODUCTION

As an imaging system, a Raman microscope technically enables the application of conventional brightfield microscopy (BFM) and Raman microspectroscopy (RMS). RMS is applied to determine the molecular structure of a sample. Spatially resolved spectral information is generated by a point-by-point mapping procedure, providing unique chemical fingerprints as a set of high-dimensional pixel vectors, which can be considered a hyperspectral image (HSI). For conventional BFM, the use of highly-corrected objectives and modern sensors with high pixel resolution ensures images of high spatial resolution. In RMS, the achieved spatial resolution depends significantly on the actual system performance and on the characteristics of the sample [1]. The focused laser spot can be considered as the point-spread function (PSF) of the image generation process, which is often disturbed by practical issues such as the complex beam guidance of the laser beam and its actual gaussian shape, leading to an effective

numerical aperture that is smaller than specified [2]. Further resolution constraints are caused by the narrow-band excitation wavelengths of the laser as well as by the sampling parameters defined by the mapping [1]. In addition, the number of sampling points is kept relatively small to avoid disproportionately long measuring times. Consequently, images formed by RMS often have a lower spatial resolution and a significantly lower pixel resolution compared to images derived from BFM. Nevertheless, they provide a higher spectral resolution and thus, contain more information for physically discriminating the sample components.

Since a Raman microscope provides images that contain complementary content in terms of high spatial and high spectral information, a combined processing might be beneficial, provided that the data sets are co-registered and compatible to a certain extent. Accordingly, this contribution addresses the problem of image fusion, aiming to form HSIs that contain both, high spectral discrimination information derived from a RMS image and high spatial resolution provided by a BFM image.

The fusion of images with corresponding properties is a well-known problem in the field of remote sensing, denoted as pansharpening [3]. Even though the imaging process in microscopy differs from that in remote sensing, the basic requirement of a correlation between the images is met since both images are acquired with sensors of similar spectral sensitivity. Thus, the application of established pansharpening methods for the fusion of images derived from RMS and BFM appears as a suitable starting point for developing a tailored solution.

The application of pansharpening algorithms for the fusion of BFM and RMS images has not yet been investigated and publications concerning other microscopy modalities are rare. In [4] J. Tarolli et al. investigated the application of a pansharpening algorithm for a fusion of secondary ion mass spectrometry (SIMS) and scanning electron microscopy (SEM). In [5] F. Vollnhals et al. compared fusion results of two different pansharpening approaches using the same modalities. In [6]

---

This work was funded by the German Research Foundation (DFG) as part of the research training group GRK 1564 *Imaging New Modalities*.

G. Franchi et al. compared the results of several established pansharpener algorithms and a new approach that was explicitly tailored to the considered microscopic images in the context of multimodal SEM fusion.

We consider this paper as a starting point to introduce the concept of pansharpener to the field of vibrational microspectroscopy and organized the remainder of this paper as follows. In Section 2, two families of pansharpener methods used within the scope of this paper are introduced and the applied algorithms are listed. Experimental results, containing information about image data generation, as well as quantitative and visual assessment of the fused images on reduced and full resolution scale are presented in Section 3. The results motivate the following discussion and conclusion in Sections 4 and 5.

## 2. PANSHARPENING ALGORITHMS

### 2.1. Component Substitution (CS) Methods

The concept of CS methods aims to separate spatial and spectral information in an upscaled HSI by transforming it into another space and to replace the component that contains the main spatial information with the panchromatic image [3]. In general, a high correlation between the replaced components is ensured by a histogram matching. By applying the inverse transformation, the data is back-projected to its original space and the fusion is completed. As shown in [7] by Tu et al., an alternative but general mathematical formulation of CS methods considering an injection scheme is given by

$$\widehat{HS}_k = \widetilde{HS}_k + g_k(\mathbf{P} - \mathbf{I}), \quad k = 1, \dots, N \quad (1)$$

where  $\widehat{HS}_k$  and  $\widetilde{HS}_k$  respectively denote the pansharpener image and the upscaled and interpolated original HSI of the  $k$ -th spectral band, the vector  $\mathbf{g} = [g_1, \dots, g_k, \dots, g_N]$  contains the injection gains,  $\mathbf{P}$  is the panchromatic image and the synthetic intensity component  $\mathbf{I}$  is defined as

$$\mathbf{I} = \sum_{i=1}^N w_i \widetilde{HS}_i \quad (2)$$

where the elements of vector  $\mathbf{w} = [w_1, \dots, w_N]$  measures the spectral overlap among the bands and the panchromatic image. Considering equations (1) and (2), the difference between the approaches that are included in the CS family mainly originate from the different procedures with which the vectors  $\mathbf{w}$  and  $\mathbf{g}$  are computed. Within the scope of this contribution, we compare four CS approaches: pansharpener based on general intensity-hue-saturation transformation (GIHS) [7], principal component analysis (PCA) [8], *adaptive* Gram-Schmidt orthogonalization (GSA) [9], as well as pansharpener by the Brovey transform (BT) [10]. For detailed mathematical descriptions, we refer to [3] and the publications referencing the mentioned approaches.

### 2.2. Multiresolution Analysis (MRA) Methods

MRA is a well-known concept from the field of image processing. Its purpose is to decompose an image iteratively into a set of images, each providing a progressively reduced resolution. Accordingly, the MRA concept in pansharpener is based on fusing the HSI with a difference image computed from the panchromatic image and its low-pass filtered version on different levels of decomposition [3]. The pansharpener image can therefore be defined by the ARSIS paradigm [3] as

$$\widehat{HS}_k = \widetilde{HS}_k + g_k(\mathbf{P} - \mathbf{P}_L), \quad k = 1, \dots, N \quad (3)$$

where  $\mathbf{P}_L$  is the low-pass filtered panchromatic image. Considering equation (3), approaches that are included in the MRA family differ according to the methods that are used to generate  $\mathbf{P}_L$  and the injection gains  $\mathbf{g}$ . The generation of  $\mathbf{P}_L$  can therefore be computed by various methods, ranging from low-pass filtering approaches to complex wavelet decompositions [3]. The following methods have been applied within this study: pansharpener based on high-pass filtering (HPF) [11], smoothing filter-based intensity modulation (SFIM) [12] and pansharpener based on a MTF-generalized low-pass filter (MTF-GLP) [13]. For a detailed description of the applied approaches, we refer to the work of Vivone et al. [3] and the publications referencing the mentioned approaches.

## 3. EXPERIMENTAL RESULTS

### 3.1. Image Data Set

The data set needed to evaluate the fusion of RMS and BFM modalities by pansharpener algorithms were generated using the Raman microscope *Senterra* developed by the *Bruker Corporation*. A microscopic sample was used, containing different polymers such as polymethylmethacrylate (PMMA) and styrene-acrylonitrile (SAN) as well as a black colorant. BFM and RMS images were generated using a  $20\times/0.4$  objective.

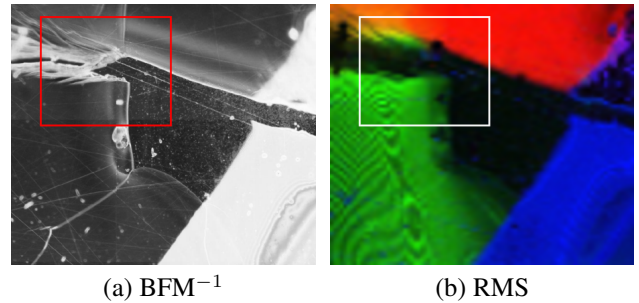


**Fig. 1:** (a) Panchromatic inverted BFM image and (b) up-scaled RMS abundance map image providing different spatial resolutions. Regions of interest are shown in Fig. 4.

While the BFM image was acquired by a  $1600 \times 1200$  pixel CMOS sensor, the RMS image was formed by applying a  $70 \times 70$  raster scan using a laser of  $785 \text{ nm}$  excitation wavelength. A CCD sensor was used to collect spectral information in terms of Raman shifts with a spectral resolution of  $0.5 \text{ cm}^{-1}$  over a wavenumber range from  $410$  to  $1790 \text{ cm}^{-1}$ . State-of-the-art preprocessing was applied to the raw data, considering outlier removal, normalization, baseline correction and spectral smoothing. The data was sub-sampled and cropped in the spectral dimension to a wavenumber range from  $410 \text{ cm}^{-1}$  to  $1490 \text{ cm}^{-1}$  to remove redundant information. To meet the requirements of the applied pansharpening algorithm and to ensure a sufficient co-registration, the RMS image was slightly upscaled to match the aspect ratio of the BFM image. Thus, a HSI of dimension  $78 \times 91 \times 542$  was used. The BFM image has been cropped to the corresponding scanning area of the RMS image. To reduce the discrepancy in terms of pixel resolution between the images, the BFM image was downscaled to a size of  $390 \times 455$  pixel.

To ensure a physically comparable interpretation of the images, the BFM image was converted into an absorption-based representation. For the visualization of the RMS and the pansharpened images, abundance maps of the three sample components were calculated by integrating over narrow bands of material specific peaks and assigning each to a channel of a conventional *RGB* image, as presented in Fig. 1(b).

### 3.2. Reduced Resolution Assessment

Reduced resolution assessment was used as the evaluation procedure for the pansharpening algorithms [3]. The original RMS data was downscaled by a factor of 2 and filtered according to a system modulation transfer function (MTF) approximation. The CS and MRA pansharpening algorithms listed in Table 1 were applied to the synthetic generated low resolution HSI and the panchromatic image that was downscaled to the size of the original RMS data.

**Table 1:** Quantitative assessment of RMS and BFM image fusion results at reduced resolution by SAM, CC, Q,  $Q2^n$  and ERGAS indices. Bold-type numbers denote the 3 best-ranked results for the corresponding index.

Method	SAM(°)	CC	Q	$Q2^n$	ERGAS
Brovey	<b>4.651</b>	0.633	0.427	0.254	21.034
MTF-GLP	5.981	0.664	<b>0.648</b>	0.441	<b>12.354</b>
GSA	<b>5.784</b>	<b>0.716</b>	<b>0.673</b>	<b>0.456</b>	<b>11.410</b>
HPF	<b>5.233</b>	<b>0.722</b>	<b>0.657</b>	<b>0.477</b>	<b>11.370</b>
GIHS	8.452	<b>0.717</b>	0.310	<b>0.474</b>	33.896
PCA	17.408	0.532	0.498	0.286	22.732
SFIM	11.386	0.011	0.624	0.275	527.473

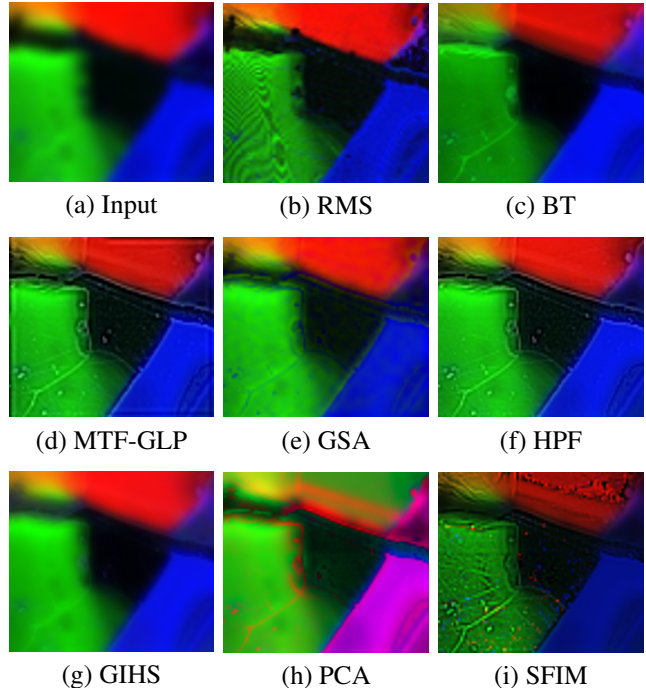


**Fig. 2:** Comparison of upscaled RMS abundance map images computed by narrow-band integration of material specific peaks for visual reduced resolution assessment. (a) Synthetic low resolution input, (b) RMS ground truth and (c)-(i) fused images, where MTF-GLP (d), GSA (e) and HPF (f) led, in accordance to the results given in Table 1, to the most convincing results.

An additional low-pass filtering that is generally applied was not conducted since, due to the high downscaling factor and the associated anti-aliasing low-pass filtering, the achieved degradation of spatial resolution was assumed to be sufficient. Accordingly, the original RMS image was used as ground truth reference image in the evaluation procedure. For a visual inspection, the abundance map images shown in Fig. 2 were used. Besides a visual assessment, the fusion product was evaluated quantitatively in terms of spatial and spectral changes using associated quality measures. The quantification of spectral distortions was determined by the spectral angle mapper (SAM), which gives the global averaged angle between pixel vectors from the pansharpened and the reference HSI. The geometric distortions was evaluated using the cross correlation (CC), which was determined for single-band images and listed as an averaged value. A further spatial assessment that takes radiometric distortions into account was performed using the averaged Q-Index. The  $Q2^n$ -Index, as its general vector extension, and the *Erreur Relative Globale Adimensionnelle de Synthèse* (ERGAS) are global indices that consider the spatial and the spectral dimension in common. All quantitative results are summarized in Table 1.

**Table 2:** Quantitative assessment of RMS and BFM image fusion results at full resolution without reference by  $D_\lambda$ ,  $D_S$  and QNR. Bold-type numbers denote the 4 best-ranked results for the QNR index.

Method	$D_S$	$D_\lambda$	QNR
<b>Brovey</b>	0.064	0.055	0.884
<b>MTF-GLP</b>	0.032	0.066	<b>0.904</b>
<b>GSA</b>	0.030	0.066	<b>0.906</b>
<b>HPF</b>	0.022	0.031	<b>0.948</b>
<b>GIHS</b>	0.038	0.135	0.832
<b>PCA</b>	0.069	0.052	0.883
<b>SFIM</b>	0.029	0.038	<b>0.935</b>

### 3.3. Full Resolution Assessment

For a full resolution assessment, CS and MRA pansharpening approaches were applied using RMS and BFM images at their original scale. No-reference quality assessment of the fusion product has been performed using the *quality w/ no reference measure* (QNR) index [3] for global evaluation. The QNR is defined as

$$\text{QNR} = (1 - D_\lambda)^\alpha (1 - D_S)^\beta \quad (4)$$

where  $D_\lambda$  quantifies the spectral and  $D_S$  the spatial distortions while  $\alpha$  and  $\beta$  are used as weighting coefficients. The QNR index and the spectral and spatial distortions measures were determined for the results of the aforementioned algorithms and are presented in Table 2. For a visual assessment, the corresponding abundance map images shown in Fig. 3 have been considered. Due to the high visual correlation that could be observed in comparison to the abundance map images shown in Fig. 2, only the results for the algorithms that provided the 4 best-ranked QNR indices are presented.

## 4. DISCUSSION

The abundance map images in Fig. 2 show that some applied pansharpening algorithms did not lead to satisfying results. PCA pansharpening shows spectral distortions artefacts that are characteristic of CS methods [14]. We assume that, in our specific case, the spatial information of the HSI is not fully included in the first principal component, which is thereby poorly correlated with the panchromatic image. The visual appearance of high spectral distortions is quantitatively confirmed by the SAM index. SFIM pansharpening shows a high spatial distortions caused by the dominance of high frequency injections while, for GIHS, the injection of spatial information was insufficient. In both cases, the spectral characteristic of the HSI was generally preserved. In comparison, BT pansharpening shows low spatial distortions, but suffers from local contrast inversion artefacts. Better results have been obtained for GSA pansharpening, where the presence of contrast

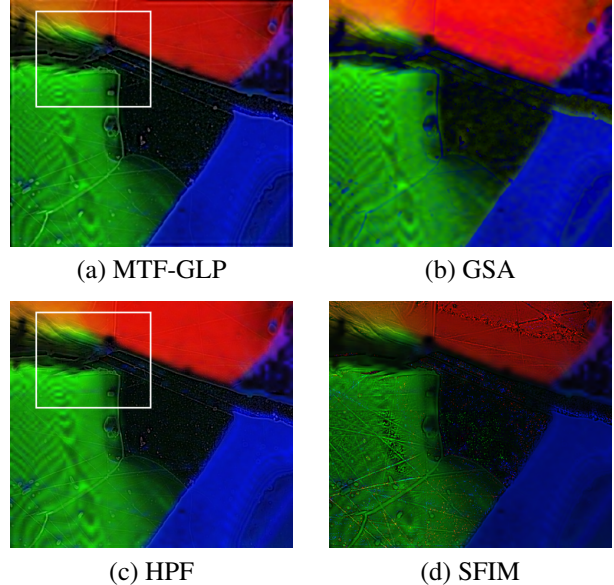


**Fig. 3:** Comparison of upscaled RMS abundance map images computed by narrow-band integration of material specific peaks for visual full resolution assessment of the fused images. Region of interest is shown in Fig.4.

inversion and spectral distortions are further reduced. From a visual point of view, MTF-GLP and HPF pansharpening showed the most convincing results for the fusion of RMS and BFM images, since both provide low spatial and spectral distortions. The good visual appearance of Fig. 2 (d), (e) and (f) is confirmed by the quantitative results presented in Table 1 as well as by the full resolution assessment, visually and quantitatively as shown in Table 2 and Fig. 3. To emphasize the good visual appearance, the regions of interest from Fig. 1 and Fig. 3 are enlarged in Fig. 4. There, it becomes evident that MTF-GLP and HPF pansharpening are spatially enhanced without causing major spectral distortions. Only slight artefacts with respect to the local contrast can be observed at edges of the sample components. They are correlated with contrast conditions in the BFM image. However, even from a chemical point of view, it can be concluded that these pansharpening algorithms complement spectral and spatial information of the sample in a meaningful way. In general, the absence of a reference image is the main drawback in the evaluation concept of pansharpening results. In a reduced resolution assessment, the choice of spatial filters is crucial while a full resolution assessment can be considered as a blind approach, where results are biased by the definition of the indices [3]. Consequently, visual assessments are still necessary. Nevertheless, using a real reference image is the most conclusive concept in image quality assessment. Thus, to enable a full resolution evaluation, we propose the generation of RMS images of higher spatial resolution by using objectives of higher numerical aperture in a finer mapping grid.

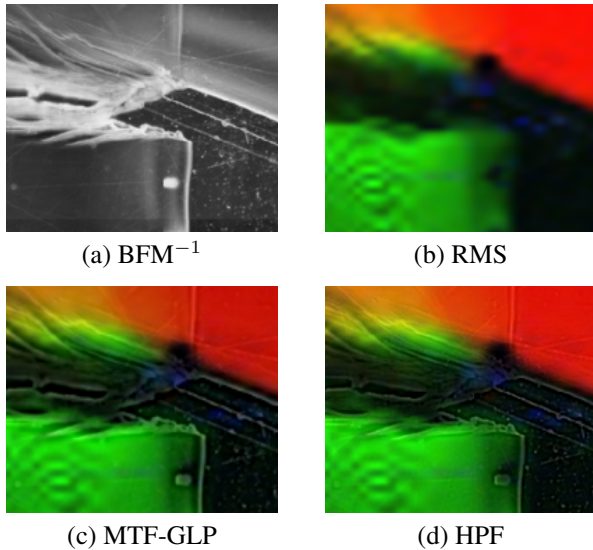


**Fig. 4:** Region of interest from Fig. 3 (a) and (c), as well as from Fig. 1 (a) and (b) for (a) BFM image, (b) RMS image, (c) MTF-GLP and (d) HPF fused images at full resolution.

## 5. CONCLUSION

This contribution investigated the application of established CS and MRA pansharpening algorithms for the fusion of BFM and RMS images with the intention of introducing the concept of pansharpening to the field of vibrational microspectroscopy. Using visual and quantitative assessment of the pansharpened images at full and reduced resolution, we found that approaches based on the MRA concept resulted in hyperspectral images of higher quality compared to those based on CS. However, the obtained results have to be confirmed by further investigations and a full reference assessment before the problem of a tailored image fusion can be addressed. Nevertheless, we assume that MRA-based algorithms are more suitable for a physical plausible fusion of RMS and BFM images and, thus, might be a better choice when developing a tailored fusion solution.

## 6. REFERENCES

- [1] E. Lee, *Raman Imaging - Techniques and Applications*, Number 168 in Springer Series in Optical Sciences. Springer-Verlag Berlin Heidelberg, 2012.
- [2] J. Trägård et al., “A simple but precise method for quantitative measurement of the quality of the laser focus in a scanning optical microscope,” *Journal of Microscopy*, vol. 259, pp. 66–73, 2015.
- [3] G. Vivone et al., “A critical comparison among pansharpening algorithms,” *IEEE Transactions on Geoscience and Remote Sensing*, vol. 53, no. 5, pp. 2565–2586, 2015.
- [4] J.G. Tarolli, H. Tian, and N. Winogard, “Application of pan-sharpening to sims imaging,” *Surf.Interface Anal.*, vol. 46, pp. 217–220, 2014.
- [5] F. Vollnhals et al., “Correlative microscopy combining secondary ion mass spectrometry and electron microscopy: Comparison of intensity-hue-saturation and laplacian pyramid methods for image fusion,” *Anal. Chem.*, vol. 259, pp. 10702–10710, 2017.
- [6] G. Franchi et al., “Enhanced edx images by fusion of multimodal sem images using pansharpening techniques,” *Journal of Microscopy*, vol. 269, pp. 94–112, 2018.
- [7] T.-M. Tu et al., “A new look at ihs-like image fusion methods,” *Inf. Fusion*, vol. 2, no. 3, pp. 177–186, 2001.
- [8] P. S. Chavez Jr. and A. W. Kwarteng, “Extracting spectral contrast in landsat thematic mapper image data using selective principal component analysis,” *Photogrammetric Engineering and Remote Sensing*, vol. 55, no. 3, pp. 339–348, 1989.
- [9] B. Aiazzi, S. Baronti, and M. Selva, “Improving component substitution pansharpening through multivariate regression of ms+pan data,” *IEEE Transactions on Geoscience and Remote Sensing*, vol. 45, no. 10, pp. 3230–3239, 2007.
- [10] A. R. Gillespie, A. B. Kahle, and R. E. Walker, “Color enhancement of highly correlated images-ii. channel ratio and chromaticity transform techniques,” *Remote Sensing of Environment*, vol. 22, no. 3, pp. 343–365, 1987.
- [11] P. S. Chavez Jr., S. C. Sides, and J. A. Anderson, “Comparison of three different methods to merge multiresolution and multispectral data: Landsat tm and spot panchromatic,” *Photogramm. Eng. Remote Sens.*, vol. 57, no. 3, pp. 295–303, 1991.
- [12] P. S. Chavez Jr., S. C. Sides, and J. A. Anderson, “Smoothing filter based intensity modulation: A spectral preserve image fusion technique for improving spatial details,” *Photogramm. Eng. Remote Sens.*, vol. 57, no. 3, pp. 295–303, 1991.
- [13] B. Aiazzi et al., “Mtf-tailored multiscale fusion of high-resolution ms and pan imagery,” *Photogramm. Eng. Remote Sens.*, vol. 72, no. 5, pp. 591–596, 2006.
- [14] C. Thomas, T. Ranchin, L. Wald, and J. Chanussot, “Synthesis of multispectral images to high spatial resolution: A critical review of fusion methods based on remote sensing physics,” *IEEE Geoscience and Remote Sensing*, vol. 46, no. 5, pp. 1301–1312, 2008.